


Microwave detection of gliding Majorana zero modes in nanowires

Olesia Dmytruk¹ and Mircea Trif²

¹*JEIP, UAR 3573 CNRS, Collège de France, PSL Research University, F-75321 Paris, France*

²*International Research Centre MagTop, Institute of Physics, Polish Academy of Sciences, Aleja Lotnikow 32/46, PL-02668 Warsaw, Poland*

 (Received 9 June 2022; revised 9 December 2022; accepted 1 March 2023; published 20 March 2023)

We study a topological superconducting nanowire that hosts gliding Majorana zero modes in the presence of a microwave cavity field. We show that the cavity decay rate depends on both the parity encoded by the Majorana zero modes and their motion, in the absence of any direct overlap of their wave functions. That is because the extended bulk states that overlap with both Majorana states facilitate their momentum-resolved microwave spectroscopy, with the gliding acting to modify the interference pattern via a momentum boost. Moreover, we demonstrate that these nonlocal effects are robust against moderate disorder in the chemical potential, and we confirm the numerical calculations with an analytical low-energy model. Our approach offers an alternative to tunneling spectroscopy to probe nonlocal features associated with the Majorana zero modes in nanowires.

DOI: [10.1103/PhysRevB.107.115418](https://doi.org/10.1103/PhysRevB.107.115418)

I. INTRODUCTION

Topological phases of matter in the context of condensed-matter physics emerged as a prominent research field following theoretical predictions of topological insulators and superconductors [1,2]. In particular, topological superconductivity is characterized by the emergence of the zero-energy bound states that are equal superpositions of electrons and holes—Majorana zero modes (MZMs) [3,4]. They obey non-Abelian statistics and are stable against disorder, making them potential building blocks for a topological quantum computer [5,6].

MZMs were predicted to emerge in a number of solid-state platforms including graphene-like systems [7–12] and chains of magnetic adatoms [13–16], with the most experimental efforts focused on semiconducting nanowires [17,18]. Over the last years, many experimental works have reported the observation of zero-bias conductance peaks [19–24] that were theoretically predicted to be a necessary signature of the presence of MZMs. However, several theoretical works have demonstrated that zero-bias conductance peaks in experimental platforms consisting of a proximitized nanowire coupled to a quantum dot [23] could arise from the trivial Andreev bound states formed in the quantum dot [25–28]. In view of the controversy associated with zero-bias peak signatures of the MZMs, alternative ways to probe MZMs are highly needed at the moment. One of the approaches going beyond local transport measurements is based on circuit quantum electrodynamics [29,30]. It has been theoretically predicted that MZMs in proximitized nanowires coupled to superconducting resonator could be probed via measuring cavity transmission coefficient [31–39]. However, these previous works that use quantum optics methods have mainly focused on static MZMs, while their dynamics, which is crucial in view of using them as topological qubits, remains largely unexplored.

Here we fill this gap and investigate the dynamics of photons in a microwave cavity coupled to a topological superconducting nanowire in the ballistic regime that hosts gliding

MZMs. We demonstrate that both the ground-state parity encoded by the MZMs and their gliding dynamics influence the cavity field decay rate into the external lines that can be accessed experimentally. We determine that these effects originate from interference processes between the localized MZMs and the extended bulk states that are being ignited by the cavity, with the gliding acting to modify the interference pattern via a momentum boost in the bulk states. This mechanism is similar to that in Refs. [40,41], where the momentum-resolved tunneling spectroscopy of a finite nanowire in the presence of a magnetic field (causing a momentum boost) reveals information about the confining potential landscape and the nature of excitations.

The paper is organized as follows. In Sec. II we introduce the model and determine the general form of the electronic susceptibility. Then, in Sec. III, we use a tight-binding approach to describe an experimentally relevant spin-orbit coupled nanowire hosting MZMs, both when they are static and when they are gliding. In Sec. IV we introduce a low-energy model that captures analytically the main features found in lattice numerics. Finally, we end in Sec. V with conclusions.

II. MODEL AND MAIN RESULTS

The Hamiltonian describing a one-dimensional topological superconductor in Fig. 1 is

$$\mathcal{H}_{\text{tot}}(t) = \frac{1}{2} \int dx \Psi^\dagger(x) [H_{el}(t) + H_{e-p}] \Psi(x) + H_p, \quad (1)$$

where $H_{el}(t)$ is the (time-dependent) Bogoliubov-de-Gennes (BdG) Hamiltonian describing the nanowire electrons, H_{e-p} is the electron-photon coupling, and $H_p = \omega_c a^\dagger a$ describes the single-mode cavity photons with the frequency ω_c and the creation (annihilation) operator a^\dagger (a). The electronic field operators can be written as $\Psi(x) = [\psi_\uparrow(x), \psi_\downarrow(x), \psi_\uparrow^\dagger(x), -\psi_\downarrow^\dagger(x)]^T$, so that the electron-photon coupling Hamiltonian reads $H_{e-p} = g(x) \tau_z (a^\dagger + a)$, with $g(x)$

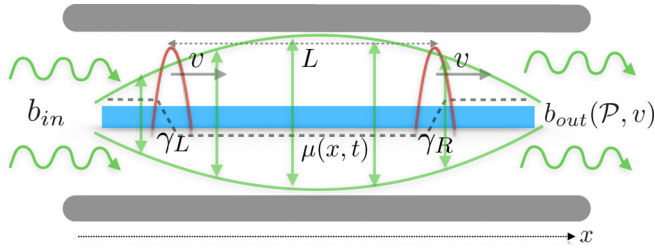


FIG. 1. Sketch of the topological superconducting nanowire-cavity system. The nanowire hosts two MZMs ($\gamma_{L,R}$) in the presence of an inhomogeneous and time-dependent chemical potential $\mu(x, t) \equiv \mu(x - vt)$. Both MZMs move with velocity v and couple to the cavity field (in green). The photons transmitted outside the cavity, b_{out} , depend on both the fermionic parity $\mathcal{P} \equiv i\langle \gamma_L \gamma_R \rangle$ defined by the two MZMs and their velocity. As described in the text, this reflects the interplay of the nonlocality of both the bulk states and the cavity field.

being the position-dependent coupling strength and τ_z being the Pauli matrix acting in the particle-hole subspace. Next, we aim to unravel the effect of the electrons on the photonic dynamics and, to keep the approach general, we do not make reference to the explicit form of $H_{el}(t)$ in this section. The equation of motion for the photonic operator up to second order in the electron-photon coupling strength $g(x)$:

$$\dot{a}(t) \approx -i[\omega_c + \chi_{el}(t, \omega_c)]a(t) - \frac{\kappa}{2}a(t) - \sqrt{\kappa}b_{in}(t), \quad (2)$$

where κ is the decay rate of the cavity, $b_{in}(t)$ is the input signal that probes the cavity, and $\chi_{el}(t, \omega_c) = (1/2\pi) \int dt' e^{i\omega_c t'} \chi_{el}(t, t')$, with [42]

$$\chi_{el}(t, t') = -i\theta(t - t') \langle [O_{el}(t, t'), O_{el}] \rangle \quad (3)$$

being the (time-dependent) electronic susceptibility associated with the operator $O_{el} = \sum_{\sigma} \int dx g(x) \psi_{\sigma}^{\dagger}(x) \psi_{\sigma}(x)$ that couples to the photons. Moreover, $O_{el}(t, t') \equiv U_{el}^{\dagger}(t, t') O_{el} U_{el}(t, t')$, with $U_{el}(t, t') = \mathcal{T} \exp[-(i/\hbar) \int_{t'}^t d\tau H_{el}(\tau)]$ being the evolution operator of the electronic system (\mathcal{T} is the time-ordering operator). Finally, $\langle \dots \rangle$ represents the expectation value with respect to the out-of-equilibrium electronic density matrix $\rho(t')$, whose derivation can, in general, be a formidable task. However, here we focus on adiabatic dynamics with respect to the topological gap Δ_t , in which case we can assume the density matrix remains unaffected by the motion [43].

We start by analyzing the case when H_{el} is time independent such that the topological nanowire harbors two distant MZMs, (e.g., due to an inhomogeneous chemical potential or magnetic field). They are described by left (right) fermionic operators $\gamma_{L(R)}$ that satisfy the Majorana condition $\gamma_{L(R)}^{\dagger} = \gamma_{L(R)}$ and encode a full fermionic state $c_M = (\gamma_L + i\gamma_R)/\sqrt{2}$ [$c_M^{\dagger} = (\gamma_L - i\gamma_R)/\sqrt{2}$] that is pinned at zero-energy in the absence of any interaction between the two end-modes. Its occupation, $n_M = c_M^{\dagger} c_M$, determines the parity of the ground state defined as

$$\hat{\mathcal{P}} = 1 - 2c_M^{\dagger} c_M = -2i\gamma_L \gamma_R, \quad (4)$$

whose expectation value, $\mathcal{P} \equiv \langle \hat{\mathcal{P}} \rangle$, can be used to describe the fidelity of the topological memory encoded in this two-dimensional subspace [3]. That is, $\mathcal{P} = \pm 1$ in a state of given parity, corresponding to a state with an even (+) or odd (−) number of electrons in the system.

The electronic susceptibility can be written as $\chi_{el}(\omega) = \chi_{el}^{MM}(\omega) + \chi_{el}^{BB}(\omega) + \chi_{el}^{BM}(\omega)$ [33], being the sum of the contribution involving the MZMs only, the bulk states only, and the cross MZM-bulk states, respectively. Since photons mediate only parity-conserving processes, $\chi_{el}^{MM}(\omega) = 0$, and, moreover, for $\omega < 2\Delta_t$, we can neglect also $\chi_{el}^{BB}(\omega)$. That is, in this frequency range, the susceptibility is dominated by the cross term (dropping the *BM* superscript from here on), which reads

$$\chi_{el}^{\mathcal{P}}(\omega) \approx \sum_{n \in \text{bulk}} \frac{|\mathcal{M}_{nL}|^2 + |\mathcal{M}_{nR}|^2 + 2\mathcal{P} \text{Im}[\mathcal{M}_{nL}^* \mathcal{M}_{nR}]}{\omega - \epsilon_n + i\eta}, \quad (5)$$

where

$$\mathcal{M}_{n\alpha} = \sum_{\sigma} \int dx g(x) [u_{\alpha\sigma}^*(x) u_{n\sigma}(x) - v_{\alpha\sigma}^*(x) v_{n\sigma}(x)],$$

are the matrix elements stemming from the local MZMs to the bulk states, with $u_{\alpha\sigma}^*(x) = v_{\alpha\sigma}(x)$ being the $\alpha = L$ and R Majorana electron and hole wave functions, while $u_{n\sigma}(x)$ [$v_{n\sigma}(x)$] are the electron (hole) weights of the bulk state with energy ϵ_n . Furthermore, η is the quasiparticle linewidth assumed, for simplicity, to be the same for all states. The above expression holds for temperatures $T \ll \Delta_t$, so that the occupation of the bulk states $p_n \approx 0$, and in the limit of negligible overlap between the MZMs $\epsilon_M \approx 0$ [for the full expression see Appendix A]. Equation (5), and in particular its imaginary part, $\text{Im}\chi_{el}^{\mathcal{P}}(\omega)$ (quantifying the absorption), represents one of our central results. It shows that the electronic susceptibility that affects the photons is sensitive to the parity encoded by two nonoverlapping MZMs via the *intensity* of the matrix elements with the extended bulk modes. For that to occur, the cavity field must cover both MZMs; otherwise, the two parities exhibit the same signal intensity.

Since these effects are rooted in the interference of the MZMs with the extended bulk states, $\delta\chi_{el}(\omega) = |\chi_{el}^+(\omega) - \chi_{el}^-(\omega)| \propto 1/L$ in the ballistic regime. This is in contrast to the detection approach scrutinized in Ref. [33] which relied on the overlap of the MZMs wave functions and resulted in a scaling $\delta\chi_{el}(\omega) \sim e^{-L/\xi}$, with $\xi = v_F/\Delta_t$ being the coherence length of the topological superconducting nanowire and v_F being the Fermi velocity. We note that the power-law scaling should persist as long as the average energy level spacing of the bulk levels ($\delta\epsilon$) satisfies $\delta\epsilon \approx v_F/L > \eta$, which can be associated with a wire length of $L^* = v_F/\eta$. Beyond this length, $\delta\chi_{el}(\omega) \sim e^{-L/L^*}$, which can be interpreted as follows: a bulk state injected at the left end has its amplitude reduced once reaching the right end because of its finite lifetime, therefore diminishing its common overlap with the two MZMs. Since typically $L^* \gg \xi$, there is a wide range of wire lengths for which these interference effects manifest such that $\epsilon_M \approx 0$.

To unravel the dynamical effects, let us assume the two MZMs are gliding rigidly, preserving the distance L between them. That can occur, for example, when the chemical

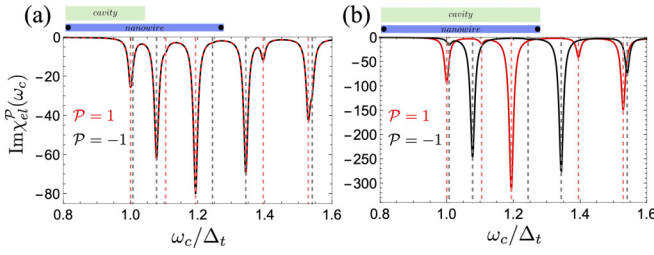


FIG. 2. Imaginary part of the susceptibility $\chi_{el}^{\mathcal{P}}(\omega)$ for parity $\mathcal{P} = \pm 1$ as a function of the cavity frequency ω_c scaled with the topological gap Δ_t . (a) The cavity couples to $N_c = 50$ sites of the nanowire and (b) the cavity couples to the nanowire over its entire length $N_c \equiv N = 100$. The red (black) line corresponds to the even (odd) parity of the MZM. The dashed vertical lines indicate the first ten resonances. In panel (a) the intensity of the transitions is the same for both parities, while in panel (b) the intensities differ substantially for $\epsilon_M \approx 0$. The other parameters are fixed as $N = 100$, $\Delta/t_h = 0.15$, $V_Z = 2.5\Delta$, $\alpha/t_h = 0.4$, $\mu = 0$, and $\eta/t_h = 10^{-3}$.

potential that imprints the topological landscape in the wire obeys $\mu(x, t) = \mu(x - vt)$, with v being the velocity of the rigid motion. Then, it is instructive to switch to the moving frame via a unitary transformation $\mathcal{W}(t) = \exp(ivpt)$ which results in the Hamiltonian $\tilde{H}_{el}(v) = H_{el}(0) - v p$. When the coupling to the cavity is constant over the length of the nanowire, $g(x) \equiv g$, the transformation $\mathcal{W}(t)$ does not affect H_{e-p} , and the susceptibility acquires the same form as in Eq. (5), but with the spectrum $\epsilon_n(v)$ and the matrix elements $\mathcal{M}_{n\alpha}$ now v dependent according to $\tilde{H}_{el}(v)$. To test these claims quantitatively, in the following we focus on a spin-orbit semiconducting nanowire (such as InAs and InSb) in proximity of an s -wave superconductor (such as Al) and subject to an external magnetic field. Such systems been recently under intense scrutiny in the quest of MZMs engineered in semiconducting nanostructures [19–24].

III. LATTICE MODEL

The minimal tight-binding Hamiltonian describing a one-dimensional nanowire composed of N lattice sites reads [44]

$$\begin{aligned}
 H_{el}(t) = & \sum_{\sigma, \sigma'} \sum_{j=1}^N c_{j, \sigma}^\dagger \{ [2t_h - \mu_j(t)] \delta_{\sigma\sigma'} + V_Z \sigma_{\sigma\sigma'}^x \} c_{j, \sigma'} \\
 & + \sum_{\sigma, \sigma'} \sum_{j=1}^{N-1} c_{j+1, \sigma}^\dagger T_{\sigma\sigma'} c_{j, \sigma'} + \sum_{j=1}^N \Delta c_{j, \uparrow}^\dagger c_{j, \downarrow}^\dagger + \text{H.c.},
 \end{aligned} \tag{6}$$

where $c_{j\sigma}^\dagger$ ($c_{j\sigma}$) is the creation (annihilation) operator acting on electrons with spin σ located at site j , $\mu_j(t)$ is the position and time-dependent chemical potential, and $t_h = \hbar^2/(2ma^2)$ is the hopping amplitude, with m and a being the effective mass and lattice constant, respectively. Here, V_Z is the Zeeman energy, $T_{\sigma\sigma'} = (i\alpha\sigma_{\sigma\sigma'}^y - t_h\delta_{\sigma\sigma'})$ is the total hopping matrix element, with α being the spin-orbit interaction (SOI) constant and $\sigma_{x,y,z}$ being the Pauli matrices acting in the spin space, while Δ is the proximity-induced superconducting pairing potential.

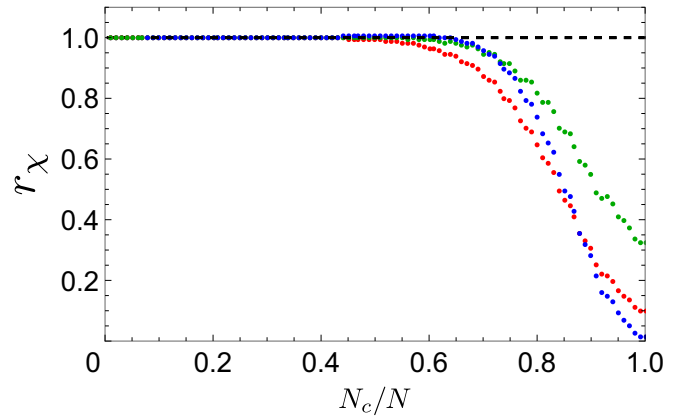


FIG. 3. Ratio of the $\mathcal{P} = \pm 1$ susceptibilities, $r_\chi = \text{Im}\chi_{el}^- / \text{Im}\chi_{el}^+$ ($r_\chi = \text{Im}\chi_{el}^+ / \text{Im}\chi_{el}^-$) for $\text{Im}\chi_{el}^- < \text{Im}\chi_{el}^+$ ($\text{Im}\chi_{el}^+ < \text{Im}\chi_{el}^-$), as a function of the fraction of sites coupled to the cavity, N_c/N . The red, green, and blue dots correspond to the first three absorption peaks. All other parameters are the same as those in Fig. 2.

We first consider a finite-size nanowire subject to a time-independent and homogeneous chemical potential μ , such that the topological gap $\Delta_t \equiv B - \sqrt{\Delta^2 + \mu^2} > 0$ and MZMs emerge at the ends of the nanowire. In our numerical simulations we focus on the strong SOI regime, $E_{\text{SO}} = m\alpha^2/(2\hbar^2) \gg V_Z$, Δ , and μ , and a nanowire with N lattice sites that result in vanishingly small zero mode splitting ($\epsilon_M/\Delta_t = 2.4 \times 10^{-6}$). We evaluated the electronic susceptibility for different ratios N_c/N , with N_c being the number of nanowire sites coupled to the microwave photons. When the photons interact with a fraction of the nanowire $N_c/N \leq 1/2$, we find that there is no discernible difference in the cavity response between the two parities $\mathcal{P} = \pm 1$, or $\delta\chi_{el}(\omega) = 0$ [see Fig. 2(a)]. However, by increasing N_c towards N , the two parities start exhibiting different intensity patterns, with the largest deviations between the two occurring when the cavity is coupled to the entire nanowire. This effect, which stems from the last terms in Eq. (5), is depicted in Fig. 2(b), where we plot the evolution of the imaginary part of the susceptibility, $\text{Im}\chi_{el}^{\mathcal{P}}$, with the cavity frequency ω_c . We note that the same features are exhibited by the real part of the susceptibility, which, however, are relegated to Appendix C. To further illustrate the difference in the susceptibility for the two parities, in Fig. 3 we show the ratio between the even- and odd-parity susceptibilities, $r_\chi = \text{Im}\chi_{el}^- / \text{Im}\chi_{el}^+$, as a function of N_c/N . Since $r_\chi < 1$ if more than half of the nanowire is coupled to the cavity, tuning the inhomogeneous coupling between the nanowire and the cavity allows one to probe the nonlocality of the MZMs. In fact, such discrimination should persist even for more pairs of nonoverlapping MZMs living in the same topological material. Additionally, such a mechanism could be utilized to initialize the nanowire in a given parity state without the requirement to fuse the two MZMs by bringing them in close proximity to each other.

In order to test the robustness of the susceptibility, we have analyzed whether disorder in the chemical potential hampers the discrimination between the parities. Here, we do not perform ensemble averaging, but instead use the quenched spatial disorder originating from the fixed random

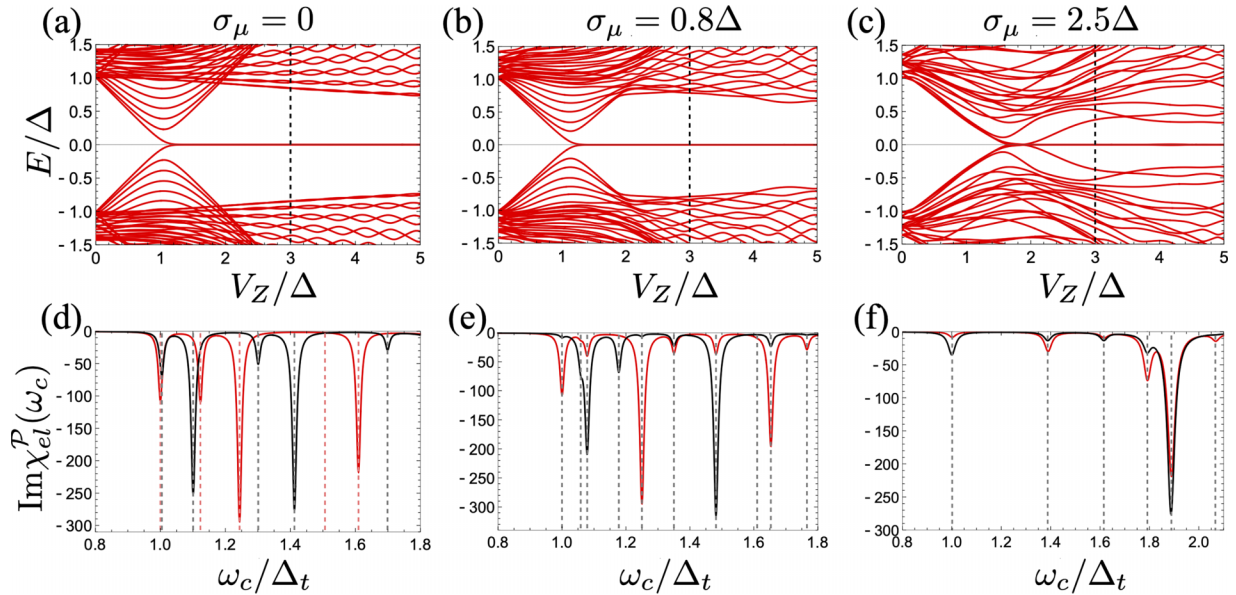


FIG. 4. (a)–(c) Energy spectrum of the finite-length disordered nanowire Eq. (6) as a function of the Zeeman energy V_Z/Δ (the value of the standard deviation σ_μ is indicated directly in the plot). (d)–(f) Imaginary part of the electronic susceptibility $\text{Im}\chi_{el}^P(\omega_c)$ as a function of the cavity frequency ω_c/Δ_t , with the topological gaps (d) $\Delta_t/\Delta = 0.88$, (e) $\Delta_t/\Delta = 0.79$, and (f) $\Delta_t/\Delta = 0.36$, for a fixed value of the Zeeman energy $V_Z/\Delta = 3$ [indicated by the black dashed line in panels (a)–(c)] and disorder in the chemical potential with the standard deviation σ_μ . The other parameters are the same as those in Fig. 2. All cases show different absorption peaks for the two parities.

configuration chosen from a Gaussian distribution, consistent with the experiment being performed at very low temperatures [45]. In Figs. 4(a)–4(c) we show the energy spectrum of Eq. (6) as a function of the Zeeman energy for three different strengths of on-site disorder in the chemical potential, with the standard deviation σ_μ . We note that zero-energy MZMs are present even for $\sigma_\mu > \Delta_t$, but with the modified bulk energy levels [see Fig. 4(c)]. Fixing the value of the Zeeman energy $V_Z/\Delta = 3$, we plot the imaginary part of the susceptibility $\text{Im}\chi_{el}^P$ as a function of the cavity frequency ω_c for different disorder strengths in Figs. 4(d)–4(f). While all the matrix elements that enter in the susceptibility are affected, we see that the two parities still exhibit significantly different intensity patterns when the on-site fluctuations in μ are smaller than the topological gap Δ_t [see Figs. 4(d) and 4(e)], while the difference in amplitudes still persists even for large values of disorder with $\sigma_\mu > \Delta_t$ [see Fig. 4(f)]. Therefore, the susceptibility remains a good quantity to harness for distinguishing between the even and the odd parities even in the presence of disorder. Our results are also consistent with previous works that demonstrate that for moderate disorder (strength smaller than Δ_t) the MZMs are largely unaffected [46–49].

To investigate the MZM dynamics, we consider a nanowire in a ring geometry that is subject to a chemical potential $\mu(j, t)$ that glides with the velocity v , such that a fraction of the ring is in the topological phase, supporting MZMs ($\Delta_t > 0$), while the rest of the ring remains in the trivial phase ($\Delta_t < 0$). To account for the gliding in the moving frame, we substitute $t_h \rightarrow t_h e^{imav}$ in the tunneling term in Eq. (6). The resulting energy spectrum of the ring in the moving frame as a function of v is depicted in the inset of Fig. 5(a). It shows that the effective gap in the energy spectrum, $\Delta_t(v)$, decreases with increasing the velocity v , with the system becoming gapless at a critical $v_c \approx \alpha$ [50]. Nevertheless, the MZMs remain

localized near zero energy up to v_c . Next, we scrutinize the evolution of the absorption peaks with the MZM dynamics. In Fig. 5(a) we show the imaginary part of the susceptibility as a function of the velocity v , exhibiting an oscillatory peak structure, similar to the dependence on ω_c in the static case. Here, the gliding of the chemical potential affects the bulk states' wave-function oscillation pattern (for a given energy ω_c), modifying their overlap with the MZMs, whose wave functions instead remain largely unaffected by v in the adiabatic limit. In Fig. 5(b) we show the frequency dependence of $\text{Im}\chi_{el}^P(\omega_c)$ at finite v . Interestingly, as compared to the static case, each resonance peak is now split into two. This feature originates from an asymmetry between the left and the right moving bulk states induced by the gliding motion of $\mu(j, t)$, absent at $v = 0$, and which alters their constructive or destructive interference.

IV. LOW-ENERGY MODEL

We can capture the essentials of the interference pattern with a low-energy continuous model describing the nanowire. The second-quantized expression for the nanowire Hamiltonian in the continuum limit is

$$\mathcal{H}_w(t) = \frac{1}{2} \int dx \Psi^\dagger(x) H_{\text{BdG}}(x, t) \Psi(x), \quad (7)$$

which it is written in terms of the Nambu spinors $\Psi(x) = \{\psi_\uparrow(x), \psi_\downarrow(x), \psi_\downarrow^\dagger(x), -\psi_\uparrow^\dagger(x)\}^T$ and with the (time-dependent) BdG Hamiltonian

$$H_{\text{BdG}} = \left(\frac{p^2}{2m} - \mu(x, t) + \alpha p \sigma_z \right) \tau_z + B \sigma_x + \Delta \tau_x, \quad (8)$$

where $\mu(x, t) \equiv \mu_0 + \delta\mu(x, t)$ is the time- and the position-dependent chemical potential that eventually induces the mo-

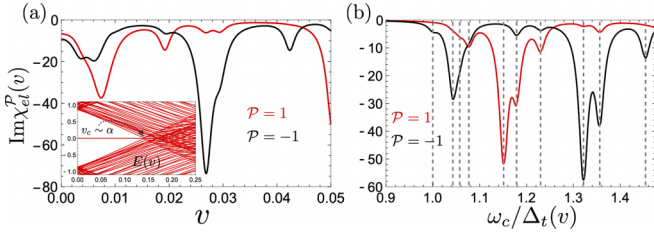


FIG. 5. (a) Imaginary part of the susceptibility $\text{Im}\chi_{el}^{\mathcal{P}}$ of the ring as a function of the velocity v for $\omega_c/\Delta = 0.9$. The red (black) line describes the even (odd) Majorana parity. Inset: Energy spectrum of the ring in the moving frame as a function of v , becoming gapless at $v \sim \alpha$. (b) Imaginary part of the susceptibility $\text{Im}\chi_{el}^{\mathcal{P}}$ of the ring as a function of the cavity frequency normalized by the effective gap $\omega_c/\Delta_t(v)$ for $v = 0.05$ [$\Delta_t(v) = 0.59\Delta$]. The red (black) line describes the even (odd) parity. The gray dashed lines indicate the position of absorption peaks. For all curves we used $V_z/\Delta = 2.5$, $N_{\text{top}} = 100$, $N_{\text{total}} = 300$, $\Delta/t_h = 0.15$, $\alpha/t_h = 0.4$, $\mu/t_h = 1.5$, and $\eta/t_h = 10^{-3}$.

tion of the MZMs. Let us define $\Delta_t(x, t) = \sqrt{\Delta^2 + \mu^2(x, t)} - B$ as the inhomogeneous topological gap, and $\mu(x, t) = \mu_0 + \delta\mu(x, t)$ such that $\Delta_t = 0$ for $\delta\mu(x, t) = 0$ (determining the positions of the MZMs). While describing the finite superconducting nanowire analytically is, in general, a difficult task, in the limit of strong SOI, quantified by $\max[\Delta_t(x, t)] \ll m\alpha^2\Delta/\mu_0B$, we can make progress following the expositions of Refs. [50,51]. First, when the system is near the topological phase transition the minimum gap occurs at $p = 0$ and we can neglect the quadratic term in Eq. (8). Second, assuming the topological region moves rigidly at finite velocity v , the pairing parameter becomes $\delta\mu(x) \rightarrow \delta\mu(x - vt)$, and we can use a unitary transformation $U(t) = e^{-ipvt}$ to gauge away the time dependence. This results in the following Hamiltonian in the moving frame:

$$\tilde{H}_{\text{BDG}}^l(x) = up\Sigma_z + \Delta_t(x, 0)\Sigma_x - vp, \quad (9)$$

with $u = \alpha\sqrt{1 - (\mu_0/B)^2}$, $p = -i\hbar\partial/\partial x$, and $\Delta_t(x) \approx \mu_0\delta\mu(x)/B$ (the corresponding high-energy Hamiltonian describes bulk states with energies larger than $\epsilon(p) > 2B$ and are disregarded from here on [51]). The Pauli matrices $\Sigma = (\Sigma_x, \Sigma_y, \Sigma_z)$ act in the space spanned by $\{(-a_+, -a_-, -a_-, a_+), (-a_-, -a_+, a_+, -a_-)\}$, with $a_{\pm} = \sqrt{1 \pm \Delta/B}$ [51]. When the system is homogeneous, i.e., $\Delta_t = \text{const}$, the eigenenergies become

$$\epsilon_{\pm}(p) = -vp \pm \sqrt{(pu)^2 + \Delta_t^2}, \quad (10)$$

which correspond to a tilted spectrum with a topological gap $\Delta_t(v) = \Delta_t(0)\sqrt{1 - \beta^2}$, where $\beta = v/u$. The system becomes gapless at $v = u$, consistent with our findings in the previous section [see inset of Fig. 5(a)]. The capacitive coupling of the electrons to the cavity effectively amounts to changes in the chemical potential μ_0 and thus acts in the low-energy sector as $H_{e-p}^l \approx g(\mu_0/B)(a^\dagger + a)\Sigma_x$. In order to obtain the electronic susceptibility in Eq. (5), we need to determine the wave functions of both the MZMs and the bulk states, respectively. For that, we utilize a scattering approach assuming the topological gap profile $\Delta_t(x) = \Delta_t$ for

$x \in (-\infty, 0) \cup (L, \infty)$, and $\Delta_t(x) = -\Delta_t$ otherwise. Consequently, in each region we can utilize linear combinations of the homogeneous space solutions and then invoke continuity of the wave functions at $x = 0$ and $x = L$. In a given region, the states with a given energy ω read as follows:

$$\psi_{\pm}(\omega, x) = \frac{1}{\mathcal{N}_{\pm}} [1, C_{\beta}(\omega \mp \sqrt{\omega^2 - 1})]^T e^{ik_{\pm}x}, \quad (11)$$

where $C_{\beta} = \text{sign}(\Delta_t)\sqrt{(1 - \beta)/(1 + \beta)}$ is a contraction factor, $k_{\pm} = (\beta\omega \pm \sqrt{\omega^2 - 1})/(u\sqrt{1 - \beta^2})$ are the two momenta for a given energy ω (for in-gap states being complex), and $\mathcal{N}_{\pm} = \sqrt{1 + C_{\beta}^2(\omega \mp \sqrt{\omega^2 - 1})^2}$ are normalization factors. All the energies above are expressed in terms of the effective gap $\Delta_t(v)$. While the scattering problem can be solved exactly for arbitrary v , the resulting expressions are lengthy and uninspiring. Instead, by solving the boundary conditions detailed in Appendix D, we can extract simple analytical expressions valid in the limits $\beta \ll 1$ and $\epsilon_M = 0$ ($L \gg u/\Delta_t$):

$$\text{Im}\chi_{el}^{\mathcal{P}} \approx \begin{cases} a(k) \cos \frac{(k-k_v)L}{2} + b(k) \sin \frac{(k-k_v)L}{2}, & \mathcal{P} = 1, \\ a(k) \sin \frac{(k-k_v)L}{2} - b(k) \cos \frac{(k-k_v)L}{2}, & \mathcal{P} = -1, \end{cases} \quad (12)$$

$$a(k) = \frac{16k^3 \sin(kL)}{(1 + k^2)^2 [k^4 + 4(1 - k^2) \sin^2(kL)]},$$

$$b(k) = \frac{16k^2 [\sin(kL) - 2k \cos(kL)]}{(1 + k^2)^2 [k^4 + 4(1 - k^2) \sin^2(kL)]}, \quad (13)$$

where $k = \sqrt{\omega^2 - 1}/u$, while $k_v = \beta\sqrt{\omega^2 - 1}/u$ is the momentum boost stemming from the gliding. We see that for $v = 0$, $\text{Im}\chi_{el}^{+(-)}(\omega) \propto \sin^4(kL/2)[\cos^4(kL/2)]$, which shows that when one parity intensity is maximum, the other parity exhibits a vanishing absorption signal, in qualitative agreement with the findings from the lattice model. In Fig. 6 we show the results for the susceptibility obtained by solving the full scattering model (from the boundary conditions), compared against the approximate results in Eq. (12) extracted for energies close to the band edge $\omega \geq \Delta_t(v)$. We see very good agreement between the two in the adiabatic limit $\beta \ll 1$. A finite v breaks this perfect alternation of maxima by inducing a momentum boost $k_v = \beta\sqrt{\omega^2 - 1}/u$ ($k_v = -\beta\sqrt{\omega^2 - 1}/u$) to the left (right) moving bulk states, affecting the interference pattern, consistent again with the numerical findings. Put differently, the extended bulk states facilitate a momentum-resolved microwave spectroscopy of the localized MZMs with the gliding acting to modify the resulting interference pattern via a momentum boost k_v [40,41].

V. CONCLUSIONS

To summarize, in this work we have shown that photons in a microwave cavity coupled to a topological superconducting nanowire that harbors MZMs are affected by both the parity of the ground state and the MZMs dynamics. These effects originate from the interference between the localized MZMs and the extended bulk states in the presence of long-range photons and do not require any overlap of the MZMs wave functions. Auspicious developments in using MZMs in

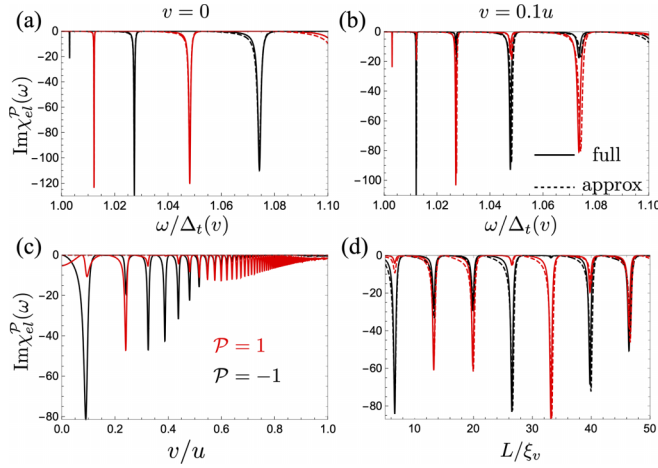


FIG. 6. The imaginary part of the susceptibility evaluated from the effective low-energy model. (a) Frequency dependence of the susceptibility for the two parities at $v = 0$. (b) Same as in panel (a) but at $v = 0.1$. (c) v dependence for $\omega = 1.1\Delta_i(0)$. (d) Dependence on the size of the topological region L scaled with the coherence length $\xi_v = 1/\Delta_i$ at $v = 0.1$. The full lines correspond to the exact result from the analytic model, while the dashed lines pertain to the approximate expressions in Eq. (12). In panels (a)–(c), we used $L = 40$, with $u = 1$ in all plots.

nanowires for quantum computing are currently hampered by the difficulty in distinguishing them from other trivial bound states. Utilizing long-range photons to map out the nonlocal structure of MZMs and their dynamics in semiconducting nanowires could offer complementary avenues to the local tunneling spectroscopy to elucidate this conundrum.

ACKNOWLEDGMENTS

This project was supported by the Foundation for Polish Science through the International Research Agendas program co-financed by the European Union within the Smart Growth Operational Programme (MAB/2017/1), and by the National Science Centre (Poland) OPUS 2021/41/B/ST3/04475 (MT). This project has received funding from the European Union's Horizon 2020 research and innovation programme under the Marie Skłodowska-Curie Grant Agreement No. 892800 (OD).

APPENDIX A: INPUT-OUTPUT FRAMEWORK

The single-mode cavity couples capacitively to the electronic density:

$$H_{e-p} = O_{el}(a^\dagger + a), \quad (\text{A1})$$

where

$$O_{el} = \sum_{\sigma} \int dx g(x) \psi_{\sigma}^{\dagger}(x) \psi_{\sigma}(x), \quad (\text{A2})$$

with $g(x)$ being the coupling strength to the electron density $\psi_{\sigma}^{\dagger}(x) \psi_{\sigma}(x)$ at position x , and a (a^\dagger) being the photon annihilation (creation) operator. The equation of motion for the photonic operator reads [52]

$$\dot{a}(t) = -i\omega_c a(t) - iO_{el,H}(t) - \frac{\kappa}{2} a(t) - \sqrt{\kappa} b_{\text{in}}(t), \quad (\text{A3})$$

where κ is the decay rate of the cavity field into the external transmission line, $b_{\text{in}}(t)$ is the input field impinging on the cavity, while $O_{el,H}(t)$ is evolved by the total Hamiltonian (Heisenberg picture). The input and output fields (which are eventually measured in an experiment) are related via

$$b_{\text{out}}(t) = b_{\text{in}}(t) + \sqrt{\kappa} a(t). \quad (\text{A4})$$

Following Ref. [42], we can write for the total density matrix $\dot{\rho}(t) = \mathcal{L}(t)\rho(t) - i[O_{el}, \rho(t)](a^\dagger + a)$, with $\mathcal{L}(t)$ being the Liouvillean of the electronic system only (but including intrinsic dissipation channels), while in the absence of the cavity the density matrix obeys $\dot{\rho}_0(t) = \mathcal{L}(t)\rho_0(t)$. Then, in leading order in the coupling to the photons, we have

$$\langle O_{el}(t) \rangle = \langle O_{el}(t) \rangle_0 + \int dt' \chi_{el}(t, t') [a(t') + a^\dagger(t')], \quad (\text{A5})$$

$$\chi_{el}(t, t') = -i\text{Tr}\{[O_{el}(t, t'), O_{el}]\rho_0(t')\}\theta(t - t'),$$

with the latter being the time-dependent electronic susceptibility measured by the cavity. Also, $O_{el}(t, t') \equiv U_{el}^\dagger(t, t') O_{el} U_{el}(t, t')$, with $U_{el}(t, t')$ being the propagator describing the unitary evolution of the system, while $\langle \dots \rangle_0$ means average with respect to $\rho_0(t)$. In Eq. (A5), we can write $a(t') \approx a(t) e^{i\omega_c(t-t')}$, which disregards higher-order corrections in the coupling to the electrons. Finally, all this allows us to write the following local in time equation for the evolution of the photonic field:

$$\begin{aligned} \dot{a}(t) &\approx -i\omega_c a(t) - i\langle O_{el}(t) \rangle_0 - ia(t) \chi_{el}(t, \omega_c) \\ &\quad - \frac{\kappa}{2} a(t) - \sqrt{\kappa} b_{\text{in}}(t), \end{aligned} \quad (\text{A6})$$

where we introduce the (time-dependent) susceptibility

$$\chi_{el}(t, \omega_c) = -i \int_{-\infty}^{\infty} dt' e^{i\omega_c t'} \chi_{el}(t, t'). \quad (\text{A7})$$

When the input field $b_{\text{in}} \gg \langle O_{el}(t) \rangle_0$, we can neglect the latter in the equation of motion, resulting in the expression shown in the paper.

In the main text, we are concerned with the dynamics induced by the gliding chemical potential $\mu(x - vt)$. The unitary transformation $\mathcal{W}(t) = \exp(ivpt)$ renders the Hamiltonian time independent:

$$\tilde{H}_{el}(t) = \mathcal{W}^\dagger(t) H_{el}(t) \mathcal{W}(t) - i\mathcal{W}^\dagger(t) \dot{\mathcal{W}}(t) \equiv H_{el}(0) - vp, \quad (\text{A8})$$

while the eigenstates in the laboratory frame and the moving frame are related by $|\psi_n(t)\rangle = \mathcal{W}(t)|\tilde{\psi}_n(t)\rangle$. The electronic evolution operator is

$$U_{el}(t, t') = \mathcal{W}^\dagger(t) e^{-i\tilde{H}_{el}(t-t')} \mathcal{W}(t'), \quad (\text{A9})$$

and the susceptibility becomes

$$\chi_{el}(t, t') = -i\text{Tr}\{[O_{el}(t, t'), O_{el}(t')]\tilde{\rho}_0(t')\}\theta(t - t'),$$

where $O_{el}(t, t') = e^{i\tilde{H}_{el}(t-t')} O_{el}(t') e^{-i\tilde{H}_{el}(t-t')}$, with $O_{el}(t) = \mathcal{W}^\dagger(t) O_{el} \mathcal{W}(t)$ and $\tilde{\rho}_0(t) = \mathcal{W}(t) \rho_0(t) \mathcal{W}^\dagger(t)$. When the cavity field is constant over the length of the nanowire (i.e., $g(x) \equiv g$), the displacement operator does not affect the coupling Hamiltonian H_{e-p} . Therefore, the combined system remains time independent in the moving frame. Assuming

adiabatic motion, we can safely assume the dynamics does not affect the density matrix, which is given by $\tilde{\rho}_0(t) \equiv \tilde{\rho}_0 = \sum_n p_n |\tilde{\psi}_n\rangle\langle\tilde{\psi}_n|$, with p_n being the occupation of the BdG levels, and which makes the susceptibility dependent only on the time difference $t - t'$. Consequently, $\chi_{el}(t, \omega) \equiv \chi_{el}(\omega)$, allowing one to determine the susceptibility analogously to the time-independent case [33].

APPENDIX B: DERIVATION OF THE ELECTRONIC SUSCEPTIBILITY

It is instructive to express the fermionic operators as follows:

$$\psi_\sigma^\dagger(x) = \sum_n [u_{n\sigma}^*(x)c_n^\dagger + v_{n\sigma}(x)c_n], \quad (\text{B1})$$

where $u_{n\sigma}(x)$ [$v_{n\sigma}(x)$] are the electron (hole) coherence factors for state n at position x and with spin σ , while c_n (c_n^\dagger) are the annihilation (creation) operators for the Bogoliubons of energy ϵ_n that diagonalize the electronic Hamiltonian in the moving frame, i.e., $\tilde{H}_{el} = \sum_n \epsilon_n (c_n^\dagger c_n - 1/2)$. Then, by employing the equation of motion $e^{i\tilde{H}_{el}t} c_n e^{-i\tilde{H}_{el}t} = c_n e^{-i\epsilon_n t}$, we can insert the above fields in the definition of O_{el} to find

$$\begin{aligned} \chi_{el}(\omega) = & \sum_{n,m} \sum_{\sigma,\tau} \int dx dx' [u_{n\sigma}^*(x)u_{m\sigma}(x) - v_{m\sigma}(x)v_{n\sigma}^*(x)] \\ & \times [u_{m\tau}^*(x')u_{n\tau}(x') - v_{n\tau}(x')v_{m\tau}^*(x')] \frac{p_n - p_m}{\omega + \epsilon_n - \epsilon_m + i\eta} \\ & + \frac{1}{2} [u_{n\sigma}^*(x)v_{m\sigma}^*(x) - u_{m\sigma}^*(x)v_{n\sigma}^*(x)] \\ & \times [v_{n\tau}(x')u_{m\tau}(x') - v_{m\tau}(x')u_{n\tau}(x')] \frac{1}{\omega + \epsilon_n + \epsilon_m + i\eta} \\ & - \frac{1}{2} [v_{n\sigma}(x)u_{m\sigma}(x) - v_{m\sigma}(x)u_{n\sigma}(x)] \\ & \times [u_{m\tau}^*(x')v_{n\tau}^*(x') - u_{n\tau}^*(x')v_{m\tau}^*(x')] \frac{1 - p_m - p_n}{\omega - \epsilon_n - \epsilon_m + i\eta}, \end{aligned}$$

where η is a small positive rate that encodes the lifetime of the levels. In this work, we are interested in the imaginary part of the susceptibility, and more specifically in energies $\omega < 2\Delta_t$. That is, we only account for the contributions that involve the bulk states and the MZMs:

$$\begin{aligned} \chi_{el}(\omega) \approx & \sum_m \left(|\mathcal{M}_{mM}^o|^2 \frac{p_M - p_m}{\omega + \epsilon_M - \epsilon_m + i\eta} \right. \\ & \left. + |\mathcal{M}_{mM}^e|^2 \frac{1 - p_m - p_M}{\omega - \epsilon_M - \epsilon_m + i\eta} \right), \quad (\text{B2}) \end{aligned}$$

where

$$\begin{aligned} \mathcal{M}_{mM}^e &= \sum_\sigma \int dx [u_{M\sigma}^*(x)u_{m\sigma}(x) - v_{M\sigma}^*(x)v_{m\sigma}(x)], \\ \mathcal{M}_{mM}^o &= \sum_\sigma \int dx [v_{M\sigma}(x)u_{m\sigma}(x) - u_{M\sigma}(x)v_{m\sigma}(x)] \quad (\text{B3}) \end{aligned}$$

are the intensities of the matrix elements describing the transitions into the bulk for the odd and even parities, respectively.

Expressing the electron and hole weights of the MZM as

$$\begin{aligned} u_{M\sigma}(x) &= \frac{1}{\sqrt{2}} [u_L^\sigma(x) + iu_R^\sigma(x)], \\ v_{M\sigma}^*(x) &= \frac{1}{\sqrt{2}} [u_L^\sigma(x) - iu_R^\sigma(x)], \quad (\text{B4}) \end{aligned}$$

readily allows us to identify the left and the right Majorana wave functions, which are separated in space and satisfy the Majorana condition $u_{L(R)\sigma}(x) = v_{L(R)\sigma}^*(x)$. With that, we can finally write

$$|\mathcal{M}_{mM}^{e,o}|^2 = |\mathcal{M}_{mL}|^2 + |\mathcal{M}_{mR}|^2 \pm 2\text{Im}[\mathcal{M}_{mL}^* \mathcal{M}_{mR}],$$

where $\mathcal{M}_{m\alpha} = \sum_\sigma \int dx [u_{\alpha\sigma}^*(x)u_{m\sigma}(x) - v_{\alpha\sigma}^*(x)v_{m\sigma}(x)]$ are the matrix elements stemming from the local Majorana $\alpha = L$ and R states and the positive energy bulk modes. The imaginary part of the susceptibility, which is responsible for the absorption peaks, reads

$$\begin{aligned} \text{Im}\chi_{el}^{e,o}(\omega) = & -\pi \sum_m \{ |\mathcal{M}_{mL}|^2 + |\mathcal{M}_{mR}|^2 \\ & \pm 2\text{Im}[(\mathcal{M}_{mL})^* \mathcal{M}_{mR}] \} \delta(\omega - \epsilon_m), \quad (\text{B5}) \end{aligned}$$

where we assumed the low-temperature regime compared to the topological gap Δ_t ($p_m \approx 0$) and the negligible Majorana overlap ($\epsilon_M \approx 0$). This shows that, while the resonance positions are the same for the two parities, their intensities differ, but only if the cavity couples to both MZMs.

APPENDIX C: NUMERICAL APPROACH FOR THE RASHBA NANOWIRE LATTICE MODEL

In this section, we provide details on the numerical evaluation of the electronic susceptibility for the tight-binding model given by Eq. (6) in the main text. To emulate the continuum analog of the gliding chemical potential, $\mu(x, t) = \mu(x - vt)$, we perform the substitution

$$t_h \rightarrow t_h e^{imav/\hbar} \quad (\text{C1})$$

in the tight-binding model in Eq. (6) in the moving frame. We are interested in cases when $\hbar/(ma) \approx v_F \gg v$, so that we can write $t_h e^{imav/\hbar} \approx t_h(1 + imav/\hbar)$. Therefore, the static electronic Hamiltonian is supplemented with the term

$$H_v = -i \frac{\hbar v}{2a} \sum_{j,\sigma} (c_{j+1\sigma}^\dagger c_{j\sigma} - c_{j\sigma}^\dagger c_{j+1\sigma}). \quad (\text{C2})$$

Diagonalizing the full Hamiltonian, including the term above, results in the spectrum presented in Fig. 5 in the main text that exhibits a gap closing at $v \approx \alpha$. For the one-dimensional ring with N sites, Eq. (6), the electronic susceptibility expressed in the moving frame reads

$$\chi_{el}(t - t') = -i\theta(t - t') \text{Tr}\{[n(t), n(t')]\tilde{\rho}_0(t')\}, \quad (\text{C3})$$

where $n = \sum_{j=1}^N c_j^\dagger c_j$ and $n(t)$ is the electron density operator in the interaction picture evolved with the total Hamiltonian, including H_v above. The density matrix was chosen as $\tilde{\rho}_0 = p_M |0\rangle\langle 0| + (1 - p_M) |1\rangle\langle 1|$, with $p_M = 0$ and 1, and $|0, 1\rangle$ being the occupation and the many-body state of parity $\mathcal{P} = -1$ and 1, respectively (we further assumed zero temperature, $T = 0$, so that all negative bulk levels are occupied).

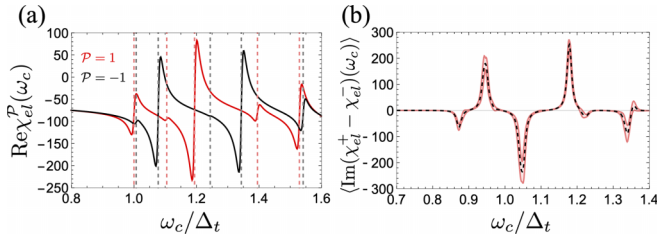


FIG. 7. (a) Real part of the total susceptibility $\text{Re}\chi_{el}^{\mathcal{P}}(\omega_c)$ as a function of the cavity frequency ω_c/Δ_t , in the topological phase ($V_Z/\Delta = 2.5$) for a finite-length nanowire homogeneously coupled to a microwave cavity. The red (black) line corresponds to the even (odd) parity of the MZMs. Pink (gray) dashed lines signal the bulk-Majorana transitions for even (odd) parity corresponding only to nonzero matrix elements. (b) Difference between the odd- and even-parity susceptibilities $\text{Im}(\chi_{el}^+ - \chi_{el}^-)$ of a nanowire with disorder in the chemical potential (standard deviation $\sigma_\mu = 0.1\Delta$) as a function of ω_c/Δ_t in the topological phase ($V_Z/\Delta = 2.5$). The black dashed line corresponds to the mean value of the difference $\text{Im}(\chi_{el}^+ - \chi_{el}^-)$ calculated for 12 disorder configurations. The pink area gives the 95% confidence interval for the population interval estimated for the difference between the two parities. The other parameters are fixed as $N = 100$, $\Delta/t_h = 0.15$, $V_Z = 2.5\Delta$, $\alpha/t_h = 0.4$, $\mu = 0$, and $\eta/t_h = 10^{-3}$.

We can make a connection to the continuum model and write H_v in terms of the instantaneous eigenstates of the Hamiltonian $H_{el}(0)$. That is, we can write

$$c_{j\sigma} = \sum_n [u_{n\sigma}(j)c_n + v_{n\sigma}(j)c_n^\dagger], \quad (\text{C4})$$

such that $H_{el}(v=0) = \sum_n \epsilon_n(v=0)(c_n^\dagger c_n - 1/2)$ and

$$H_v = -i\frac{\hbar v}{2} \sum_{j,\sigma} \sum_{n,m} [\partial_j u_{n\sigma}^*(j)c_n^\dagger + \partial_j v_{n\sigma}^*(j)c_n] \\ \times [u_{m\sigma}(j)c_m + v_{m\sigma}(j)c_m^\dagger] - \text{H.c.} \equiv -i\frac{\hbar}{2} \sum_j \mathbf{c}^\dagger \mathbf{R}^\dagger \partial_j \mathbf{R} \mathbf{c},$$

where $\mathbf{c} = (c_1, c_2, \dots, c_1^\dagger, c_2^\dagger, \dots)$ and $\mathbf{R}(t)$ is the matrix whose columns are eigenvectors of $H_{el}(0)$. Furthermore, we have defined $\partial_j u_{n\sigma} \equiv [u_{n\sigma}(j+1) - u_{n\sigma}(j)]/a$ [and similarly for $\partial_j v_{n\sigma}(j)$], while the time derivative is to be understood as $\partial_t \mathbf{R} \equiv v \sum_j \partial_j \mathbf{R}$.

In Fig. 7(a) we plot the real part of the susceptibility $\text{Re}\chi_{el}^{\mathcal{P}}(\omega_c)$ for a finite-length nanowire with $N = 100$ lattice sites. We note that $\text{Re}\chi_{el}^{\mathcal{P}}(\omega_c)$ exhibits different oscillation patterns for the two parities, similarly to the imaginary part of the susceptibility $\text{Im}\chi_{el}^{\mathcal{P}}(\omega_c)$ described in the main text. This contribution $\text{Re}\chi_{el}^{\mathcal{P}}(\omega_c)$ alters the cavity resonance frequency. To further demonstrate that the susceptibility remains a good quantity to distinguish between two parities even in the presence of disorder, we evaluate the difference $r_\chi \equiv \langle \text{Im}(\chi_{el}^+ - \chi_{el}^-) \rangle$ for a disordered nanowire averaged over 12 disorder realizations of the chemical potential. In Fig. 7(b) we show the disorder-averaged r_χ as a function of the cavity frequency ω_c . We note that the susceptibility for two parities has different intensities when the on-site fluctuations in μ are smaller than the topological gap Δ_t . Therefore, the susceptibility could be

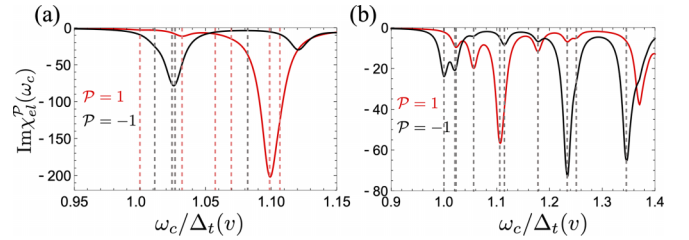


FIG. 8. Imaginary part of the total susceptibility $\text{Im}\chi_{el}^{\mathcal{P}}(\omega_c)$ of the superconducting ring as a function of the cavity frequency normalized by the velocity-dependent topological gap $\omega_c/\Delta_t(v)$ for (a) $v = 0$ [$\Delta_t(v)/\Delta_t = 0.86$] and (b) $v = 0.025$ [$\Delta_t(v)/\Delta_t = 0.74$]. The red (black) line corresponds to the even (odd) parity of the MZMs. The pink (gray) dashed lines indicate the positions of the peaks in $\text{Im}\chi_{el}^{\mathcal{P}}(\omega_c)$ for even (odd) parity. The other parameters are fixed as $V_Z/\Delta = 2.5$, $N_{\text{top}} = 100$, $N_{\text{total}} = 300$, $\Delta/t_h = 0.15$, $\alpha/t_h = 0.4$, $\mu/t_h = 1.5$, and $\eta/t_h = 10^{-3}$.

utilized to distinguish between the even and the odd parities even when we average over various disorder realizations.

Additionally, in Fig. 8 we show $\text{Im}\chi_{el}^{\mathcal{P}}(\omega_c)$ for a nanowire in a ring geometry for two different values of the velocity v compared to Fig. 5 in the main text. We find that the number and the position of the peaks in $\text{Im}\chi_{el}^{\mathcal{P}}(\omega_c)$ are modified for finite values of v due to the modification of the nanowire bulk wave functions.

APPENDIX D: ANALYTICAL MODEL IN THE STRONG SOI REGIME

Here we provide more details on the derivation of the susceptibility in the continuum model. The electronic fields $\Psi_l(x) = [\psi_{l,u}(x), \psi_{l,d}(x)]$ associated with the low-energy BdG Hamiltonian

$$\tilde{H}_{\text{BdG}}^l(x) = up\Sigma_z + \Delta_l(x, 0)\Sigma_x - vp \quad (\text{D1})$$

are

$$\psi_{l,u}(x) = -a_+[\psi_\uparrow(x) + \psi_\uparrow^\dagger(x)] - a_-[\psi_\downarrow(x) + \psi_\downarrow^\dagger(x)], \\ \psi_{l,d}(x) = -a_-[\psi_\uparrow(x) - \psi_\uparrow^\dagger(x)] - a_+[\psi_\downarrow(x) - \psi_\downarrow^\dagger(x)], \quad (\text{D2})$$

and $\psi_{l,u(d)}^\dagger(x) = +(-)\psi_{l,u(d)}^\dagger(x)$. Therefore, the second-quantized interaction Hamiltonian between the cavity and the electronic density becomes

$$\mathcal{H}_{e-p}^l \approx \frac{2g\mu_0}{B} \int dx \psi_{l,u}(x)\psi_{l,d}(x)(a^\dagger + a). \quad (\text{D3})$$

We can express these fermionic fields in terms of the eigen-Bogoliubons for a given chemical potential landscape:

$$\psi_{l,u}(x) = \sum_n [U_n(x)c_n + U_n^*(x)c_n^\dagger], \quad (\text{D4})$$

$$\psi_{l,d}(x) = \sum_n [V_n(x)c_n - V_n^*(x)c_n^\dagger], \quad (\text{D5})$$

where $U_n(x)$ and $V_n(x)$ are the electronic weights of the state n associated with the eigen-Bogoliubons c_n that diagonalize the nanowire Hamiltonian, and which can in turn be written as

$$c_n = \int dx [U_n^*(x)\psi_{l,u}(x) + V_n^*(x)\psi_{l,d}(x)]. \quad (\text{D6})$$

For the MZM instead, we can write it as $c_M = (\gamma_L + i\gamma_R)/\sqrt{2}$, with $\gamma_{L,R}^\dagger = \gamma_{L,R}$ being the corresponding left and right Majorana fermion operators, with the explicit expressions

$$\gamma_L = \int dx \left[\underbrace{[U_M^*(x) + U_M(x)]}_{U_L(x)} \psi_{l,u}(x) + \underbrace{[V_M^*(x) - V_M(x)]}_{iV_L(x)} \psi_{l,d}(x) \right], \quad (D7)$$

$$\gamma_R = \int dx \left[\underbrace{[U_M^*(x) - U_M(x)]/i}_{U_R(x)} \psi_{l,u}(x) + \underbrace{[V_M^*(x) + V_M(x)]/i}_{iV_R(x)} \psi_{l,d}(x) \right]. \quad (D8)$$

To evaluate the susceptibility, we employ several approximations. First, we only retain the cross terms involving MZMs and bulk states, and we neglect the purely bulk contribution, focusing on frequencies $\omega < 2\Delta_t$. Moreover, we assume the nanowire to be long enough such that the MZM splitting $\epsilon_M \approx 0$. Then, the susceptibility takes the form in Eq. (B2), with

$$\begin{aligned} \mathcal{M}_{nM}^e &= -\left(\frac{2g\mu_0}{B}\right)^2 \int dx [U_M^*(x)V_n^*(x) - V_M^*(x)U_n^*(x)], \\ \mathcal{M}_{nM}^o &= -\left(\frac{2g\mu_0}{B}\right)^2 \int dx [U_M(x)V_n^*(x) + V_M(x)U_n^*(x)]. \end{aligned} \quad (D9)$$

To determine the electron and hole weights in the above expressions, we consider the following topological landscape (in the moving frame):

$$\Delta_t(x) = \begin{cases} \Delta_t, & x \in (-\infty, 0) \cup (L, \infty), \\ -\Delta_t, & x \in [0, L], \end{cases} \quad (D10)$$

$$\psi_M(x) = \begin{cases} a_M [1, C(\beta)(E + i\sqrt{1-E^2})]^T e^{ip-x}, & x < 0, \\ b_M [1, -C(\beta)(E + i\sqrt{1-E^2})]^T e^{ip-x} + c_M [1, -C(\beta)(E - i\sqrt{1-E^2})]^T e^{ip+x}, & x \in [0, L], \\ d_M [1, C(\beta)(E - i\sqrt{1-E^2})]^T e^{ip+(x-L)}, & x > L, \end{cases} \quad (D16)$$

from where the in-gap spectrum can be found by imposing the continuity of the wave function at $x = 0$ and $x = L$ and that the determinant formed by the coefficients vanishes. We obtain

$$\epsilon_M = e^{-\frac{\sqrt{1-\epsilon_M^2}}{u\sqrt{1-\beta^2}}L}, \quad (D17)$$

and

$$b_M = \frac{ia_M\epsilon_M}{\sqrt{1-\epsilon_M^2}}, \quad (D18)$$

with L being the size of the middle part of the nanowire. Therefore, in a given region the wave function pertaining to the Hamiltonian in Eq. (D1) (traveling or evanescent) can be written as

$$\psi_{\pm}(E, x) = \begin{pmatrix} U_{\pm}(E) \\ V_{\pm}(E) \end{pmatrix} e^{ip_{\pm}(E)x}, \quad (D11)$$

where

$$p_{\pm}(E) = \frac{\beta E \pm \sqrt{E^2 - 1}}{u\sqrt{1 - \beta^2}}, \quad (D12)$$

$$V_{\pm}(E) = \text{sign}(\Delta_t)C(\beta)(E \mp \sqrt{E^2 - 1})U_{\pm}(E), \quad (D13)$$

with $\beta = v/u$ and $C(\beta) = \sqrt{\frac{1-\beta}{1+\beta}}$ being a contraction factor. Note that the effective gap is $\Delta_t(v) = |\Delta_t|\sqrt{1-\beta^2}$, and all energies above are expressed in terms of $\Delta_t(v)$. However, the boundaries will lead to mixing of these pristine states with a given energy. In the following, we evaluate the degree of mixing using a scattering approach, both for the in-gap states as well as for the traveling modes.

1. In-gap Majorana modes

To find the spectrum and the wave functions of the in-gap modes, we set $|E| < \Delta_t(v)$. Then

$$V_{\pm}(E) = \text{sign}(\Delta_t)C(\beta)(E \mp i\sqrt{1-E^2})U_{\pm}(E). \quad (D14)$$

with the two (complex) momenta at energy E being

$$p_{\pm}(E) = k_v(E) \pm i\kappa(E), \quad (D15)$$

where $k_v(E) = \beta E/(u\sqrt{1-\beta^2})$ and $\kappa_v(E) = \sqrt{1-E^2}/(u\sqrt{1-\beta^2})$. Consequently, the wave function (keeping only the terms that do not diverge at $\pm\infty$) can be written as

$$c_M = a_M \left(1 - \frac{i\epsilon_M}{\sqrt{1-\epsilon_M^2}} \right), \quad (D19)$$

$$d_M = a_M (\epsilon_M + i\sqrt{1-\epsilon_M^2}). \quad (D20)$$

Finally, a_M can be found from the normalization condition of the in-gap states $\int_{-\infty}^{\infty} dx |\psi_M(x)|^2 = 1$, which gives

$$|a_M| \approx \frac{1}{2} \sqrt{\frac{C(\beta)}{u}}. \quad (D21)$$

2. Extended bulk states

In this case $|E| > \Delta_r(\beta)$, and we have to account for both the left (+) and the right (-) moving states,

$$V_{\pm}(E) = \text{sign}(\Delta_r)C(\beta)(E \mp \sqrt{E^2 - 1})U_{\pm}(E) \quad (\text{D22})$$

and

$$p_{\pm}(E) = \frac{\beta E \pm \sqrt{E^2 - 1}}{u\sqrt{1 - \beta^2}}, \quad (\text{D23})$$

while the normalization of the states gives

$$U_{\pm}(E) = [1 + C^2(\beta)(2E^2 - 1 \mp 2E\sqrt{E^2 - 1})]^{-1/2}. \quad (\text{D24})$$

The positive energy solutions for the states traveling from left to right read as follows:

$$\Psi_+(E, x) = \begin{cases} U_+(E)[1, C(\beta)(E - \sqrt{E^2 - 1})]^T e^{ip_+x} + a_E^+[1, C(\beta)(E + \sqrt{E^2 - 1})]^T e^{ip_-x}, & x < 0, \\ b_E^+[1, -C(\beta)(E - \sqrt{E^2 - 1})]^T e^{ip_+x} + c_E^+[1, -C(\beta)(E + \sqrt{E^2 - 1})]^T e^{ip_-x}, & x \in [0, L], \\ d_E^+[1, C(\beta)(E - \sqrt{E^2 - 1})]^T e^{ip_+x}, & x > L, \end{cases} \quad (\text{D25})$$

and similarly for the states impinging on the topological region from the left:

$$\Psi_-(E, x) = \begin{cases} a_E^-[1, C(\beta)(E + \sqrt{E^2 - 1})]^T e^{ip_-x}, & x < 0, \\ b_E^-[1, -C(\beta)(E - \sqrt{E^2 - 1})]^T e^{ip_+x} + c_E^-[1, -C(\beta)(E + \sqrt{E^2 - 1})]^T e^{ip_-x}, & x \in [0, L], \\ U_-(E)[1, C(\beta)(E + \sqrt{E^2 - 1})]^T e^{ip_-x} + d_E^-[1, C(\beta)(E - \sqrt{E^2 - 1})]^T e^{ip_+x}, & x > L. \end{cases} \quad (\text{D26})$$

By imposing the continuity of the wave functions at $x = 0$ and L , we can determine all the scattering coefficients a_E^{\pm} , b_E^{\pm} , c_E^{\pm} , and d_E^{\pm} . Inserting the above wave functions in

Eq. (D9) allows us to calculate fully analytically the susceptibility and to extract the expressions showed in the main text.

[1] M. Z. Hasan and C. L. Kane, Colloquium: Topological insulators, *Rev. Mod. Phys.* **82**, 3045 (2010).

[2] X.-L. Qi and S.-C. Zhang, Topological insulators and superconductors, *Rev. Mod. Phys.* **83**, 1057 (2011).

[3] A. Y. Kitaev, Unpaired Majorana fermions in quantum wires, *Phys.-Usp.* **44**, 131 (2001).

[4] C. Beenakker, Search for Majorana fermions in superconductors, *Annu. Rev. Condens. Matter Phys.* **4**, 113 (2013).

[5] A. Y. Kitaev, Fault-tolerant quantum computation by anyons, *Ann. Phys.* **303**, 2 (2003).

[6] C. Nayak, S. H. Simon, A. Stern, M. Freedman, and S. Das Sarma, Non-Abelian anyons and topological quantum computation, *Rev. Mod. Phys.* **80**, 1083 (2008).

[7] J. Klinovaja, S. Gangadharaiah, and D. Loss, Electric-field-induced Majorana Fermions in Armchair Carbon Nanotubes, *Phys. Rev. Lett.* **108**, 196804 (2012).

[8] J. Klinovaja, G. J. Ferreira, and D. Loss, Helical states in curved bilayer graphene, *Phys. Rev. B* **86**, 235416 (2012).

[9] A. M. Black-Schaffer, Edge Properties and Majorana Fermions in the Proposed Chiral d -Wave Superconducting State of Doped Graphene, *Phys. Rev. Lett.* **109**, 197001 (2012).

[10] J. Klinovaja and D. Loss, Giant Spin-Orbit Interaction Due to Rotating Magnetic Fields in Graphene Nanoribbons, *Phys. Rev. X* **3**, 011008 (2013).

[11] P. San-Jose, J. L. Lado, R. Aguado, F. Guinea, and J. Fernández-Rossier, Majorana Zero Modes in Graphene, *Phys. Rev. X* **5**, 041042 (2015).

[12] V. Kaladzhyan and C. Bena, Formation of Majorana fermions in finite-size graphene strips, *SciPost Phys.* **3**, 002 (2017).

[13] S. Nadj-Perge, I. K. Drozdov, B. A. Bernevig, and A. Yazdani, Proposal for realizing Majorana fermions in chains of magnetic atoms on a superconductor, *Phys. Rev. B* **88**, 020407(R) (2013).

[14] J. Klinovaja, P. Stano, A. Yazdani, and D. Loss, Topological Superconductivity and Majorana Fermions in RKKY Systems, *Phys. Rev. Lett.* **111**, 186805 (2013).

[15] B. Braunecker and P. Simon, Interplay between Classical Magnetic Moments and Superconductivity in Quantum One-Dimensional Conductors: Toward a Self-Sustained Topological Majorana Phase, *Phys. Rev. Lett.* **111**, 147202 (2013).

[16] M. M. Vazifeh and M. Franz, Self-Organized Topological State with Majorana Fermions, *Phys. Rev. Lett.* **111**, 206802 (2013).

[17] R. M. Lutchyn, J. D. Sau, and S. Das Sarma, Majorana Fermions and a Topological Phase Transition in Semiconductor-Superconductor Heterostructures, *Phys. Rev. Lett.* **105**, 077001 (2010).

[18] Y. Oreg, G. Refael, and F. von Oppen, Helical Liquids and Majorana Bound States in Quantum Wires, *Phys. Rev. Lett.* **105**, 177002 (2010).

[19] V. Mourik, K. Zuo, S. M. Frolov, S. Plissard, E. P. Bakkers, and L. P. Kouwenhoven, Signatures of Majorana fermions in hybrid superconductor-semiconductor nanowire devices, *Science* **336**, 1003 (2012).

[20] M. Deng, C. Yu, G. Huang, M. Larsson, P. Caroff, and H. Xu, Anomalous zero-bias conductance peak in a Nb-InSb nanowire-Nb hybrid device, *Nano Lett.* **12**, 6414 (2012).

- [21] A. Das, Y. Ronen, Y. Most, Y. Oreg, M. Heiblum, and H. Shtrikman, Zero-bias peaks and splitting in an Al-InAs nanowire topological superconductor as a signature of Majorana fermions, *Nat. Phys.* **8**, 887 (2012).
- [22] H. O. H. Churchill, V. Fatemi, K. Grove-Rasmussen, M. T. Deng, P. Caroff, H. Q. Xu, and C. M. Marcus, Superconductor-nanowire devices from tunneling to the multichannel regime: Zero-bias oscillations and magnetoconductance crossover, *Phys. Rev. B* **87**, 241401(R) (2013).
- [23] M. Deng, S. Vaitiekėnas, E. B. Hansen, J. Danon, M. Leijnse, K. Flensberg, J. Nygård, P. Krogstrup, and C. M. Marcus, Majorana bound state in a coupled quantum-dot hybrid-nanowire system, *Science* **354**, 1557 (2016).
- [24] M. W. A. de Moor, J. D. S. Bommer, D. Xu, G. W. Winkler, A. E. Antipov, A. Bargerbos, G. Wang, N. Van Loo, R. L. M. Op het Veld, S. Gazibegovic *et al.*, Electric field tunable superconductor-semiconductor coupling in Majorana nanowires, *New J. Phys.* **20**, 103049 (2018).
- [25] C.-X. Liu, J. D. Sau, T. D. Stanescu, and S. Das Sarma, Andreev bound states versus Majorana bound states in quantum dot-nanowire-superconductor hybrid structures: Trivial versus topological zero-bias conductance peaks, *Phys. Rev. B* **96**, 075161 (2017).
- [26] A. Ptok, A. Kobińska, and T. Domański, Controlling the bound states in a quantum-dot hybrid nanowire, *Phys. Rev. B* **96**, 195430 (2017).
- [27] C. Reeg, O. Dmytruk, D. Chevallier, D. Loss, and J. Klinovaja, Zero-energy Andreev bound states from quantum dots in proximitized Rashba nanowires, *Phys. Rev. B* **98**, 245407 (2018).
- [28] R. Hess, H. F. Legg, D. Loss, and J. Klinovaja, Local and non-local quantum transport due to Andreev bound states in finite Rashba nanowires with superconducting and normal sections, *Phys. Rev. B* **104**, 075405 (2021).
- [29] A. Blais, R.-S. Huang, A. Wallraff, S. M. Girvin, and R. J. Schoelkopf, Cavity quantum electrodynamics for superconducting electrical circuits: An architecture for quantum computation, *Phys. Rev. A* **69**, 062320 (2004).
- [30] A. Wallraff, D. I. Schuster, A. Blais, L. Frunzio, R.-S. Huang, J. Majer, S. Kumar, S. M. Girvin, and R. J. Schoelkopf, Strong coupling of a single photon to a superconducting qubit using circuit quantum electrodynamics, *Nature (London)* **431**, 162 (2004).
- [31] M. Trif and Y. Tserkovnyak, Resonantly Tunable Majorana Polariton in a Microwave Cavity, *Phys. Rev. Lett.* **109**, 257002 (2012).
- [32] A. Cottet, T. Kontos, and B. Douçot, Squeezing light with Majorana fermions, *Phys. Rev. B* **88**, 195415 (2013).
- [33] O. Dmytruk, M. Trif, and P. Simon, Cavity quantum electrodynamics with mesoscopic topological superconductors, *Phys. Rev. B* **92**, 245432 (2015).
- [34] O. Dmytruk, M. Trif, and P. Simon, Josephson effect in topological superconducting rings coupled to a microwave cavity, *Phys. Rev. B* **94**, 115423 (2016).
- [35] M. C. Dartiailh, T. Kontos, B. Douçot, and A. Cottet, Direct Cavity Detection of Majorana Pairs, *Phys. Rev. Lett.* **118**, 126803 (2017).
- [36] A. Cottet, M. C. Dartiailh, M. M. Desjardins, T. Cubaynes, L. C. Contamin, M. Delbecq, J. J. Viennot, L. E. Bruhat, B. Douçot, and T. Kontos, Cavity QED with hybrid nanocircuits: from atomic-like physics to condensed matter phenomena, *J. Phys.: Condens. Matter* **29**, 433002 (2017).
- [37] M. Trif, O. Dmytruk, H. Bouchiat, R. Aguado, and P. Simon, Dynamic current susceptibility as a probe of Majorana bound states in nanowire-based Josephson junctions, *Phys. Rev. B* **97**, 041415(R) (2018).
- [38] M. Trif and P. Simon, Braiding of Majorana Fermions in a Cavity, *Phys. Rev. Lett.* **122**, 236803 (2019).
- [39] L. Contamin, M. Delbecq, B. Douçot, A. Cottet, and T. Kontos, Hybrid light-matter networks of Majorana zero modes, *npj Quantum Inf.* **7**, 171 (2021).
- [40] O. M. Auslaender, A. Yacoby, R. de Picciotto, K. W. Baldwin, L. N. Pfeiffer, and K. W. West, Tunneling spectroscopy of the elementary excitations in a one-dimensional wire, *Science* **295**, 825 (2002).
- [41] Y. Tserkovnyak, B. I. Halperin, O. M. Auslaender, and A. Yacoby, Finite-Size Effects in Tunneling between Parallel Quantum Wires, *Phys. Rev. Lett.* **89**, 136805 (2002).
- [42] S. Kohler, Dispersive Readout of Adiabatic Phases, *Phys. Rev. Lett.* **119**, 196802 (2017).
- [43] T. Albash, S. Boixo, D. A. Lidar, and P. Zanardi, Quantum adiabatic Markovian master equations, *New J. Phys.* **14**, 123016 (2012).
- [44] D. Rainis, L. Trifunovic, J. Klinovaja, and D. Loss, Towards a realistic transport modeling in a superconducting nanowire with majorana fermions, *Phys. Rev. B* **87**, 024515 (2013).
- [45] H. Pan and S. Das Sarma, Disorder effects on majorana zero modes: Kitaev chain versus semiconductor nanowire, *Phys. Rev. B* **103**, 224505 (2021).
- [46] P. W. Brouwer, M. Duckheim, A. Romito, and F. von Oppen, Probability Distribution of Majorana End-State Energies in Disordered Wires, *Phys. Rev. Lett.* **107**, 196804 (2011).
- [47] P. W. Brouwer, M. Duckheim, A. Romito, and F. von Oppen, Topological superconducting phases in disordered quantum wires with strong spin-orbit coupling, *Phys. Rev. B* **84**, 144526 (2011).
- [48] A. M. Lobos, R. M. Lutchyn, and S. Das Sarma, Interplay of Disorder and Interaction in Majorana Quantum Wires, *Phys. Rev. Lett.* **109**, 146403 (2012).
- [49] J. D. Sau and S. Das Sarma, Density of states of disordered topological superconductor-semiconductor hybrid nanowires, *Phys. Rev. B* **88**, 064506 (2013).
- [50] M. S. Scheurer and A. Shnirman, Nonadiabatic processes in Majorana qubit systems, *Phys. Rev. B* **88**, 064515 (2013).
- [51] T. Karzig, G. Refael, and F. von Oppen, Boosting Majorana Zero Modes, *Phys. Rev. X* **3**, 041017 (2013).
- [52] A. A. Clerk, M. H. Devoret, S. M. Girvin, F. Marquardt, and R. J. Schoelkopf, Introduction to quantum noise, measurement, and amplification, *Rev. Mod. Phys.* **82**, 1155 (2010).